Energy Storage Materials 50 (2022) 543–553

Contents lists available at ScienceDirect

Energy Storage Materials

journal homepage: www.elsevier.com/locate/ensm

Operando electrochemical pressiometry probing interfacial evolution of electrodeposited thin lithium metal anodes for all-solid-state batteries

Haechannara Lim [a], Seunggoo Jun [a], Yong Bae Song [a], Hongyeul Bae [b], Jin Hong Kim [b,*], Yoon Seok Jung [a,*]

[a] Department of Chemical and Biomolecular Engineering, Yonsei University, Seoul 03722, South Korea
[b] Battery Materials Research Center, Research Institute of Industrial Science & Technology (RIST), Pohang 37673, South Korea

ARTICLE INFO

Keywords:
Solid-state batteries
thin Li metal anodes
Operando pressiometry
Interfacial evolution

ABSTRACT

All-solid-state Li metal batteries with ultimate energy density require stabilization at the Li/solid electrolyte interfaces. Further, the use of conventional thick (hundreds of μm) Li metal anodes (LMAs) hinders an impartial evaluation of full cells. In this study, interfacial evolution is compared for thin LMAs (~ 10 μm thick) prepared by a scalable electrodeposition, with varying protective In/Li_xIn layer formed via electroless plating. The positive effects of the In/Li_xIn layer are confirmed for both Li/Li_6PS_5Cl/Li symmetric cells and $LiNi_{0.70}Co_{0.15}Mn_{0.15}O_2$/$Li_6PS_5Cl$/Li full cells. Complementary analysis including electrochemical, ex situ X-ray photoelectron spectroscopy, operando electrochemical pressiometry, and cross-sectional scanning electron microscopy measurements discloses complex Li/Li_6PS_5Cl interfacial evolutions affected by the In/Li_xIn coatings, that is, suppressed side reactions and penetrating Li growth. Importantly, a new indicator from operando electrochemical pressiometry analysis, the capacity-normalized pressure change difference $\Delta(\Delta P_Q)$ successfully predicts the dendritic growth of Li during cycling of $LiNi_{0.70}Co_{0.15}Mn_{0.15}O_2$/Li full cell.

1. Introduction

Electrification of power trains and energy storage systems have boosted research on lithium-ion batteries (LIBs) with higher energy density [1,2]. Accordingly, specific and volumetric energy densities of the state-of-the-art LIBs have reached ~260 W h kg^{-1} and ~770 W h L^{-1}, that are more than doubled ever since their first introduction to the commercial market in the early 1990s [1–3]. Further leap in energy density requires the adaptation of Li metal anode (LMA) owing to its highest theoretical capacity (3860 mA h g^{-1} or 2061 mA h cm^{-3}) and the lowest potential (−3.04 V vs. the normal hydrogen electrode (NHE)) [4-8]. However, the practical applications of LMAs have been hindered by their extreme vulnerability toward internal short circuits (ISCs) and aggressive reactivity with conventional organic liquid electrolytes, which are detrimental to their safety performance [4-10]. To circumvent the limitations related to liquid electrolytes and safety concerns, and to enable the utilization of LMAs, all-solid-state Li metal batteries (ASLMBs) using non-flammable inorganic solid electrolytes (SEs) have been investigated extensively [11-18]. Till date, various types of inorganic SEs with high Li^+ conductivities of at least 10^{-3} S cm^{-1} at room temperature, including sulfides (e.g., $Li_{5.5}PS_4Cl_{1.5}$: 12 mS cm^{-1}) [19,20], oxides (e.g., $Li_7La_3Zr_2O_{12}$: 0.1–1 mS cm^{-1}) [21], halides (e.g., Li_3YCl_6: 0.5 mS cm^{-1}) [22–24], and closo-borates (e.g., $0.7Li(CB_9H_{10})-0.3Li(CB_{11}H_{12})$: 6.7 mS cm^{-1}) [24,25], have been widely investigated for ASLMBs.

However, SEs have not fully stabilized LMAs. First of all, Li metals grow by penetrating into the SEs during Li plating [17,18,27–29]. Voids at interfaces and defects such as cracks and grain boundaries of SEs, can act as the pathways for the penetrating Li growth. In addition, insufficiently low electronic conductivity of SEs could cause the Li nucleation inside the SE layer [16]. The growing dendritic Li eventually leads to an ISC and sudden death of cells [27,29]. Furthermore, LMAs experience significant volume changes during repetitive charge–discharge cycles, with 5.0 μm of thickness change corresponding to 1.0 mA h cm^{-2}. In particular, SEs are reductively decomposed while in contact with Li metal and form passivating solid electrolyte interphases (SEIs) comprising poor ion-conducting byproducts, such as Li_2S and Li_3P [30-33]. The uncontrolled growth of these passivation layers reconfigures the interfacial contacts between the LMA and SE and consequently increases the cell impedance, which has a detrimental effect on the cell

* Corresponding authors.
E-mail addresses: jinhong.kim@rist.re.kr (J.H. Kim), yoonsjung@yonsei.ac.kr (Y.S. Jung).

https://doi.org/10.1016/j.ensm.2022.05.050
Received 7 March 2022; Received in revised form 15 May 2022; Accepted 26 May 2022
Available online 27 May 2022

performance. In addition, interfacial contact loss can induce current constriction, which facilitates the penetration of Li [27,29-34].

Various surface modification strategies have been attempted to address interfacial instability problems of LMAs in ASLMBs. i) Engineering artificial SEIs based on inorganic Li compounds can efficiently stabilize Li-SE interfaces [35-38]. Inorganic SEIs possessing high interface energy with Li metal and robust physical property successfully suppressed the dendritic Li growth [38]. ii) Conformal metal coatings lead to stabilized interfaces by preventing direct contact between Li and SEs [34,39,40]. Further, it was shown that the application of bifunctional interphase with Li_xMg alloy and LiF stabilized the LMA-SE interfaces [41]. iii) Using Ag-C composite anodes, Li metal was grown in situ at the Ag-C/current collector interfaces, thereby bypassing the direct contact between Li and SEs [42].

In addition, a critical limitation to the practical applications of LMAs is the thickness of the Li metal. To achieve the targeted energy densities (~400 W h kg^{-1} and 1000 W h L^{-1}) of rechargeable Li batteries, thin LMAs should be utilized [43–46]. Even under optimized cell conditions with high-mass-loading cathodes and thin SE membranes, ASLMBs with massive Li reservoirs (~200 μm thick) provide only limited energy densities of up to 300 W h kg^{-1} and 400 W h L^{-1} (Fig. 1a, a detailed calculation of energy densities is given in the Supporting Information). The value of 400 W h L^{-1} is even lower than that of the latest LIBs (~770 W h L^{-1}). LMAs with thicknesses less than 10 μm provide the targeted values for both gravimetric and volumetric energy densities of ASLMBs. However, the majority of previous studies on ASLMBs have utilized thick Li foils (e.g., ~1 mm thickness) and suffered from impractical energy density level [13,17,37,38,43,44,47–50]. Additionally, thick LMAs can act as infinite reservoir of Li and this hinders a fair evaluation of the battery systems. Specifically, even though Li is continuously lost due to

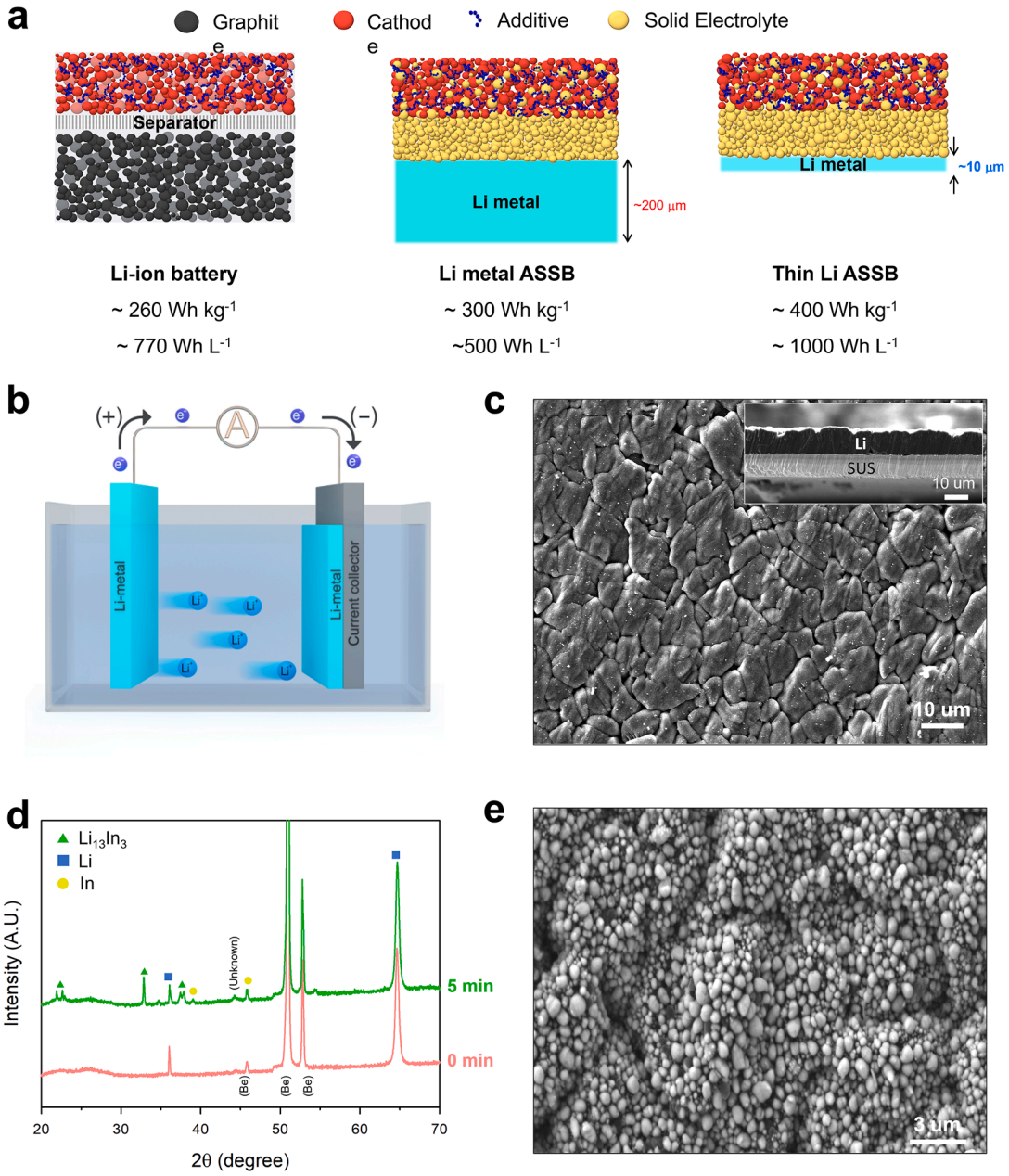

Fig. 1. Electrodeposited thin LMAs for high-energy ASLMBs. (a) Comparison of cell configuration and energy densities for LIBs, ASLMBs using thick and thin Li metal anodes. (b) Schematic of the electrodeposition process for thin LMAs. (c) Top SEM image of the electrodeposited thin LMA. Cross-sectional SEM image is also shown in the inset of (c). (d) XRD patterns of Li metals before (0 min) and after the In/Li_xIn coatings (5 min). (e) SEM image of the In/Li_xIn LMA.

side reactions, the cycling performance is not affected by Li losses because the thick LMAs act as an almost limitless Li reservoir [47,51,52]. In contrast, Li loss can pose great impact on cyclability when thin LMAs with limited amount of Li reservoir are used. Therefore, application of promising protective layers and understanding their effects on interfacial evolution are in urgent need for improving the performance of ASLMBs.

Based on the aforementioned issues and challenges, herein, we report a facile and scalable electrodeposition method for fabricating thin LMAs (~ 10 μm thick Li deposited on a stainless steel (SUS) current collector) and their stabilization via electroless In plating using an indium bis(trifluoromethanesulfonyl)imide ($In(TFSI)_3$) solution [53]. Symmetric cells of Li/Li_6PS_5Cl (LPSCl)/c-Li (c-Li refers to a counter electrode of $Li_{100}In$ (nominal composition, weight ratio of Li to In is 8:2)) and $LiNi_{0.70}Co_{0.15}Mn_{0.15}O_2$ (NCM)/LPSCl/Li all-solid-state full cells demonstrated enhanced cycling stability after optimizing the In/Li_xIn coatings on the electrodeposited thin LMAs. Further, electrochemical, cross-sectional scanning electron microscopy (SEM), ex situ X-ray photoelectron spectroscopy (XPS), revealed that In/Li_xIn coatings suppressed detrimental side reactions at the Li/LPSCl interfaces and the penetration of Li growth into SE layer, which was also confirmed by operando electrochemical pressiometry analysis. Specifically, it is demonstrated that a new indicator for internal short circuit, that is, a capacity-normalized pressure change difference $\Delta(\Delta P_Q)$, can probe the Li plating mechanism.

2. Results and discussion

Thin LMAs (~10 μm thick Li) were prepared using a facile and scalable electrodeposition process (Fig. 1b). Li metal was electrodeposited on a SUS foil (~10 μm thick) using a solution of 3 M LiFSI in 1,2 dimethoxyethane (DME) with a targeted thickness as thin as ~10 μm and an area of 100 × 100 mm^2. The SEM and photograph images of the top surface (Figs. 1c and S1a) showed smooth surfaces without any major defects in the electrodeposited Li layers. The thickness measurement results obtained for the entire area of the thin LMA and the cross-sectional SEM image showed a uniform distribution of 10.5–11.5 μm (Figures S1b, c and the inset of Fig. 1c). The X-ray diffraction (XRD) pattern of the electrodeposited LMAs showed two characteristic reflections for metallic Li at 36° and 65° (PDF no.15–0401) without any signals of impurities or unknown phases (Fig. 1d, denoted as 0 min). The Li 1s XPS spectrum of the electrodeposited LMA showed the presence of Li metal with LiF, Li_2CO_3, and Li_2O impurities (Figure S2) derived from the LiFSI/DME solution. Notably, the electrodeposition protocol for LMAs demonstrated herein (Fig. 1b) has the potential for mass production via a roll-to-roll process, as illustrated in Figure S3. Moreover, electrodeposition strategy has advantages compared to mechanical rolling, liquid phase processes and Li metal powder method in terms of cost, purity and yield as well (Table S1).

Electroless plating of In was applied to the electrodeposited thin LMAs to stabilize the Li/SE (LPSCl) interface in all-solid-state cells. Electroless In deposition proceeded by soaking the as-electrodeposited LMA in a solution of 12 mM $In(TFSI)_3$ in a mixture of ethylene carbonate (EC) and dimethyl carbonate (DMC) (1:1, v/v) [53]. Owing to the large difference in the standard electrode potential between Li/Li^+ (−3.04 V vs. NHE) and In/In^{3+} (−0.34 V vs. NHE) [54,55], the displacement reaction ($3Li^0 + In^{3+} \rightarrow 3Li^+ + In^0$, $\Delta G^o = -847.27$ kJ/mol) is favored, and it resulted in the coating of metallic In species on Li metal surfaces via the consumption of Li (Figure S4) [53,56]. The soaking time determined the amount and morphology of the coating layers, and it was optimized to 5 min, as discussed later. After the electroless In plating, the surface of LMAs (a sample plated for 5 min was denoted as the 5 min sample) turned gray from the light yellow color of the pristine sample (the 0 min sample) (Figure S5). The electroless-plated coating layers for the 5 min LMA sample were probed by XRD, XPS, and SEM measurements. The XRD pattern of the electroless-plated LMA confirmed the Li-In alloy phase ($Li_{13}In_3$, pdf. No.65–6908) and In metal, in addition to trace amounts of unknown impurities (Fig. 1d). The electroless-plated LMA samples were referred to as In/Li_xIn-coated LMAs. The Li 1s and In 3d XPS spectra of the In/Li_xIn-coated LMA are displayed in Figure S6a, and b, respectively. The Li 1s spectrum exhibited the signals for $Li_{13}In_3$ and Li metal at 55.4 and 52.8 eV, respectively, and those for Li_2CO_3 and Li_2O, which are the solution-derived byproducts (Figure S6a) [57]. In the In 3d spectrum (Figure S6b) strong peaks for In metal (442.2 and 450.2 eV) and In_2O_3 (444.5 and 453.5 eV) with the signals for $Li_{13}In_3$ alloy phase (443.2 and 451.2 eV) were observed [58]. An SEM image of the In/Li_xIn-coated LMA and the corresponding energy dispersive X-ray spectroscopy (EDXS) elemental map of In are shown in Figs. 1e and S7, respectively. Compared to the morphology of the as-electrodeposited uncoated LMA (0 min, Fig. 1c), it can be seen that submicron globular In/Li_xIn particles cover the entire Li surface (Fig. 1e). The EDXS elemental map of In indicated the uniform distribution of the coating materials (Figure S7).

The electroless In plating was optimized by varying the soaking time of the bare LMAs in the $In(TFSI)_3$ solutions from 5 to 15 and 40 min. The results of the Li/LPSCl/c-Li symmetric cells at 60 °C, are compared in Fig. 2. The positive voltage profiles correspond to the plating of Li^+ from the counter electrode (c-Li) on the working electrode (electrodeposited thin Li) while the negative voltage profiles correspond to the stripping of Li^+ from the working electrode to the counter. At a current density of 1 mA cm^{-2} with a capacity of 1 mA h cm^{-2} for each charge and discharge, the 5 min sample exhibited the lowest polarization and the longest cycle life of up to 540 h (Fig. 2a). This result is in contrast to that of the uncoated LMA (cycle life of up to 320 h). As we applied thin Li metal (~10 μm) as a working electrode with a limited capacity of 2 mA h cm^{-2} which is in contrast to the excessive amount of Li reservoir of c-Li, depletion of Li reservoir occurs at the working electrode (thin Li metal) and thus causes a sharp increase of overpotential during the Li stripping stage (negative voltage profiles) in the later part of cycling, as shown in Fig. 2a. Nyquist plots for the uncoated and In/Li_xIn-coated LMAs, corresponding to the stripping/deposition tests in Fig. 2a are shown for different cycles in Fig. 2b, and they were fitted with the equivalent circuit model shown in Figure S8. The corresponding results are summarized and plotted in Table S2, Fig. 2c, and Figure S9 respectively. R_1, which corresponds to the x-axis intercepts of the Nyquist plots, represents the resistance of the LPSCl layer (Figure S10). The $R_2 + R_3$ values indicate the overall interfacial resistances for Li/SE [30,59]. In particular, the uncoated LMAs (0 min) showed significantly decreasing R_1 values as the cycling proceeded from 7.4 to 4.6 Ω, and then from 4.6 to 4.1 Ω after 60 and 110 cycles, respectively (Fig. 2c). This observation is interpreted to be a consequence of the penetrating growth of Li metal into the SE layers [16–37]. Further, the interphase and interfacial resistance ($R_2 + R_3$) increased upon cycling, from 4.5 to 7.9 Ω, and then from 7.9 to 10.4 Ω after 60 and 110 cycles, respectively, indicating that excessive side reactions occurred and caused great amount of SEI formation at the Li/LPSCl interfaces (Figure S9) [30,59]. In contrast, the SE layer resistance (R_1) for the In/Li_xIn-coated LMAs (5 min) decreased only during the initial 60 cycles (from 9.5 to 8.6 Ω) and remained saturated at ~8.5 Ω (Fig. 2c). The decrease in R_1 for the In/Li_xIn-coated LMAs in this work was much smaller (−1.0 Ω up to 210th cycle) compared to that for the uncoated LMAs (−3.4 Ω up to 110th cycle), substantiating the suppressed penetrating growth of Li by the In/Li_xIn coating. Furthermore, the growth of the total interfacial resistance ($R_2 + R_3$) was reduced by the In/Li_xIn coating, indicating its advantageous role in suppressing Li/LPSCl interfacial reactions (Table S2). Overall, the results for the symmetric cells (Fig. 2a–c) demonstrate that the In/Li_xIn coating layers suppress the decomposition of LPSCl and the penetrating growth of Li. Further, increment tests were carried to determine the critical current density which implies the maximum endurable current density for ASLMB without ISC [60]. Li/LPSCl/c-Li symmetric cells were cycled with fixed cycling times by continuously increasing the current density and capacity every three cycles at 30 °C and 60 °C (FigureS11)

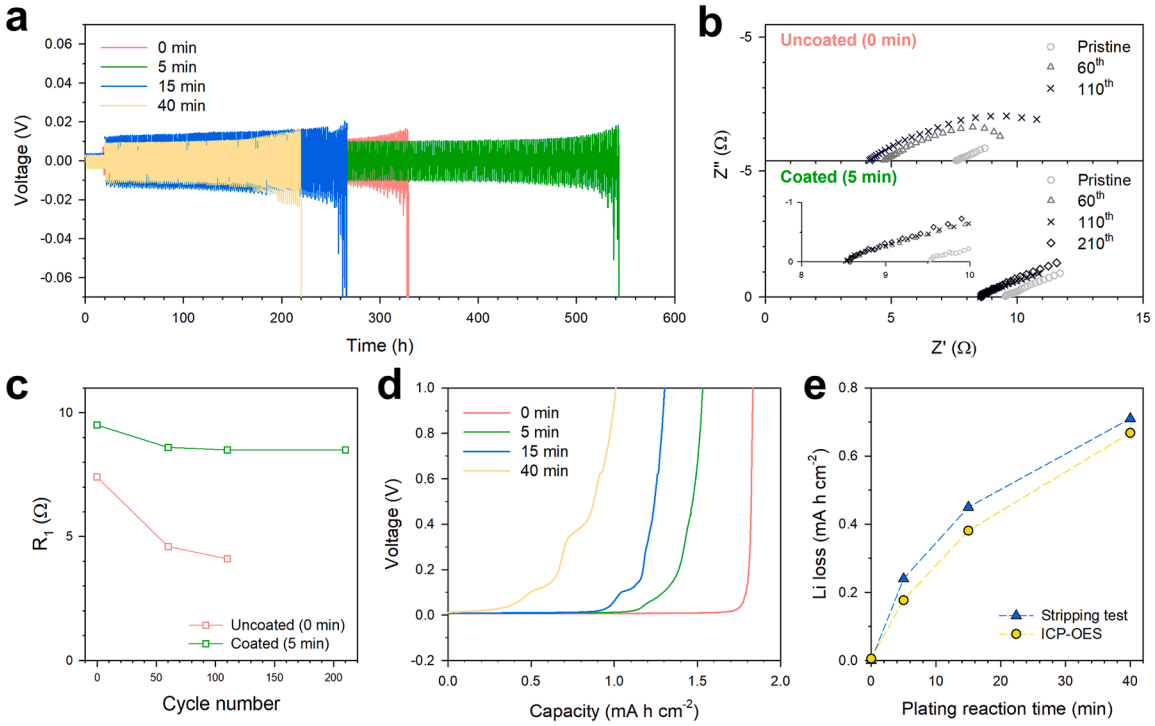

Fig. 2. Results of In/Li_xIn-coated LMAs with varying the electroless plating reaction time. (a) Galvanostatic cycling of Li/LPSCl/c-Li cells using In/Li_xIn-coated LMAs. (b) Nyquist plots of c-Li/LPSCl/Li cells using uncoated (0 min) and Li/Li_xIn-coated (5 min) LMAs, and (c) corresponding R_1 values as a function of cycle number. (d) Initial discharge (delithiation) voltage profiles of c-Li/LPSCl/Li cells using In/Li_xIn-coated LMAs. (e) Amount of Li consumed by the electroless plating reaction, determined by the stripping test and ICP-OES measurements.

[60]. However, the In/Li_xIn coatings on LMAs did not show prominent improvements. Both the uncoated and In/Li_xIn-coated samples exhibited ISCs at 3–4 mA cm^{-2} at 60 °C and at 1.5 mA cm^{-2} at 30 °C.

Despite the remarkably enhanced performance of the 5 min sample, the samples with prolonged reaction times of 15 and 40 min showed even shorter cycle lives of 260 and 220 h, respectively, compared to the 0 min (or uncoated) sample (320 h) (Fig. 2a). First, as the electroless plating of In consumes Li, a longer reaction time leads to a larger amount of Li loss, and the amount of remaining Li metal can significantly impact the performance of ASLMBs. The amount of Li loss was quantified by both stripping tests and inductively coupled plasma–optical emission spectrometry (ICP-OES) measurements (Fig. 2d and e, and Table S3). The growth rate of In metal during electroless plating is provided in Supporting Information. Not surprisingly, an inverse relationship between the remaining Li capacity and the plating reaction time was confirmed. The 0 min sample showed a total capacity of 1.84 mA h cm^{-2}, which is consistent with the theoretical capacity of 10 μm thick Li metal (2.0 mA h cm^{-2}). After the electroless plating reaction for 5, 15, and 40 min, the remaining Li capacities determined by the stripping tests, decreased to 1.60, 1.39, and 1.13 mA h cm^{-2}, respectively. The ICP-OES results agree well with the stripping test results. Furthermore, the surface morphology of the In/Li_xIn layers could be another factor that affects electrochemical performance. To promote even Li^+ fluxes during deposition, the surface morphology should be uniform without any protrusions or the uncontrolled presence of coating particles. In contrast to the uniform and fine coating materials for the 5 min sample (Fig. 1e), the longer plating reaction resulted in coarser and irregular shapes (Figure S12). The inhomogeneous distribution of In/Li_xIn particles on the Li surface could easily cause large local current densities and consequently uneven deposition of Li metal. In summary, although the In/Li_xIn coatings avoid direct contact between Li and LPSCl and suppress the side reactions, the excessive plating reaction time resulted in a large amount of Li loss and irregular and uneven morphologies of the coatings, which are disadvantageous for stable cycling. This could explain the optimal performance of the 5 min sample.

To further validate the effect of the In/Li_xIn protective layer, the Li/LPSCl interfacial evolution after cycling of Li/LPSCl/c-Li symmetric cells was probed for the 0 min and 5 min samples by ex situ XPS and striping measurements (Fig. 3). The Li 1s and S 2p XPS spectra are shown in Fig. 3a and b, respectively, and the fitted results are summarized in Table S4. For the 0 min sample after 110 cycles, significant chemical decomposition of LPSCl was observed in both Li 1 s and S 2p spectra with obvious evolution of the peaks at 56.5 (Li 1s), and 160.5 and 161.5 eV (S 2p) for Li_2S which is a well-known Li-sulfide SE byproduct [30–32, 63–66]; the areal fraction for Li_2S signals with respect to Li_6PS_5Cl was much smaller for the cycled 5 min sample, compared to those for the cycled uncoated sample (0 min): 0.37 vs. 4.35 for Li 1s signal and 0.15 vs. 0.73 for S 2p signal. In addition, reaction between In and LPSCl may form additional interfacial byproducts such as In_2S_3 [61,62]. However, due to the close peak positions for In_2S_3 (161.6 eV) and Li_6PS_5Cl (161.7 eV), clear-cut deconvolution was not possible [61].

The side-reaction suppression ability of the In/Li_xIn layer was also confirmed by the Li stripping test results (Fig. 3c and d). After 110 cycles, the remaining Li capacities were measured and are summarized in Table 1. The uncoated LMA (0 min) showed a capacity drop from 1.84 to 1.19 mA h cm^{-2} after 110 cycles, corresponding to 35% of Li loss, which is attributed to the amount of the Li/LPSCl side reaction. By applying the In/Li_xIn protective layer (5 min), the capacity drop after 110 cycles was decreased to half, i.e., only 18% (from 1.60 to 1.33 mA h cm^{-2}). Therefore, the ex situ XPS and stripping test results confirm the effectiveness of the In/Li_xIn coatings for the suppression of Li/LPSCl side reactions upon repeated cycling.

To assess the effects of In/Li_xIn-coated thin LMAs under practical full cell configuration, NCM/Li all-solid-state full cells for uncoated (0 min) and coated (5 min) LMAs were tested in the voltage range of 3.0–4.3 V at 60 °C, and the results are shown in Figs. 4a and b, and S13–S15. Using the In/Li_xIn-coated LMA, NCM/Li full cells showed an initial discharge capacity of 166 mA h g^{-1} at 1.0 C and stable cycle life up to 200 cycles

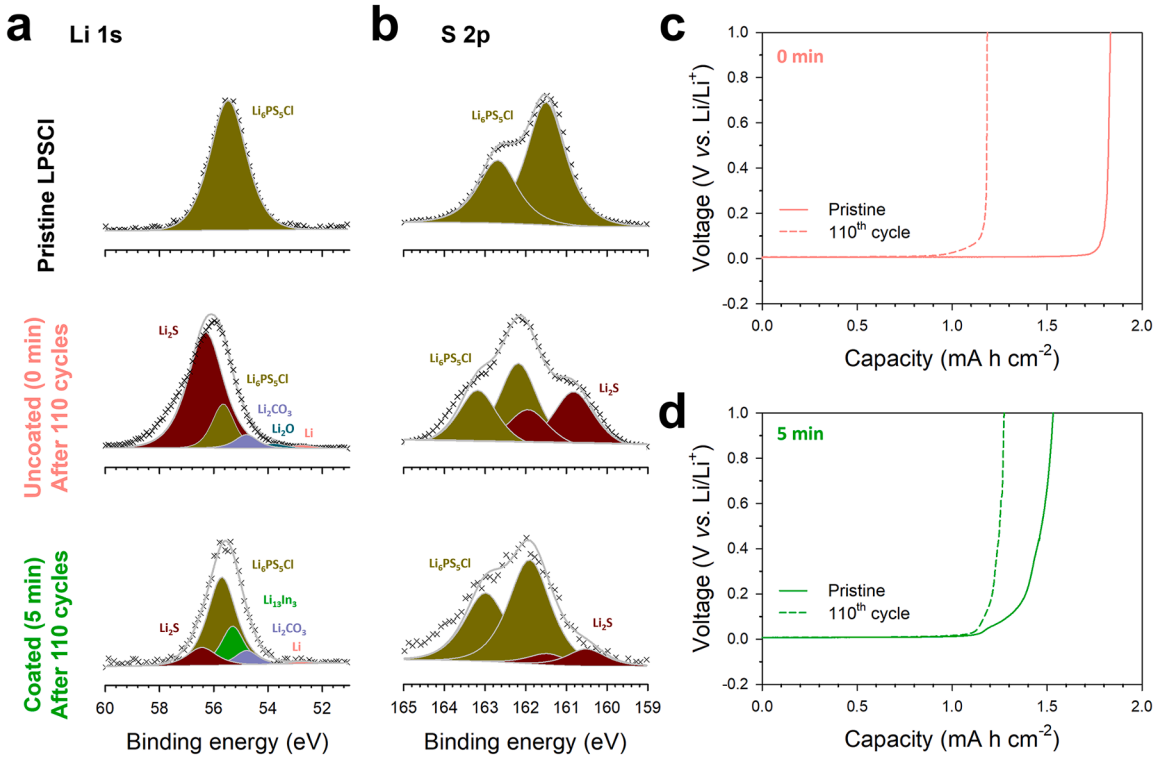

Fig. 3. Ex situ XPS signals of (a) Li 1s and (b) S 2p for pristine LPSCl and LPSCl after 110 cycles with uncoated (0 min) and In/Li_xIn-coated (5 min) LMAs. Discharge capacities for (c) uncoated (0 min) and (d) In/Li_xIn-coated (5 min) LMAs before cycling and after 110 cycles.

Table 1
Li capacities for uncoated (0 min) and In/Li_xIn-coated (5 min) LMAs before and after cycling of Li/LPSCl/c-Li symmetric cells at 60 °C.

Sample (electroless plating reaction time)	Li reservoir capacity (mA h cm^{-2})	
	Before cycling	After 100 cycles
0 min (uncoated)	1.84	1.19 (35.3% loss)
5 min	1.60	1.33 (17.8% loss)

with 79% capacity retention and 98.92% average coulombic efficiency (Fig. 4a). In contrast, the full cells using the unprotected LMA showed a smaller capacity of 150 mA h g^{-1} and sudden death by ISC only in the 32nd cycle. A similar trend was also observed in the full cells cycled at 0.5 C (Figure S15). Compared with the result of the Li/LPSCl/c-Li symmetric cells lasting up to 320 h (or 160 cycles, Fig. 2a), the much shorter cycle life ended with ISC of the NCM/Li full cells (Fig. 4a) is significant. ISCs were more frequently observed from NCM/Li full cells due to a couple of distinctive features from Li symmetric cells. First, the areal capacities of the NCM/Li full cells were larger (1.4 or 2.4 mA h cm^{-2}) than those of the symmetric cells (1 mA h cm^{-2}). Second, the thick counter electrode (~100 mA h cm^{-2}) for the symmetric cells, unlike NCM cathode with only limited Li amount, supplies an almost unlimited amount of Li despite the significant consumption of Li at the LMA/LPSCl interfaces by side reactions [49]. Therefore, the drastic difference in cycling performance between the Li/LPSCl/c-Li symmetric cells and NCM/Li full cells is implied. Further, the rate capabilities of the uncoated and In/Li_xIn-coated LMAs are shown in Figures S13b and 4b, respectively. The superior cycling performance of the NCM/Li full cells using the In/Li_xIn-coated LMAs, compared to that of the uncoated LMAs, is emphasized, particularly in terms of the suppressed interfacial side reaction and consequently Li loss, which also counteract the penetrating growth of Li.

Reducing the capacity ratio of the negative to positive electrodes (N/P ratio) to unity or even smaller values is an important prerequisite for ASLMBs with energy densities higher than 400 W h kg^{-1} [46]. However, reducing the N/P ratio leads to a limited Li source to compensate for the side-reaction-derived Li loss, as discussed when comparing the symmetric and full cells above [49]. Therefore, an evaluation of the LMA performance with a practically acceptable low N/P ratio (i.e., <1) is essential [49,67]. In Fig. 4c and Table S5, the cycling performances for all-solid-state full cells from previous studies in terms of N/P ratios against cycle numbers are compared. Notably, most previous studies have reported results with N/P ratios of ≥ ~10 [48-50,68-70]. In contrast, our results demonstrated excellent cycling performances with practically acceptable N/P ratios of 1.53 or 1.02 owing to the coupling of exceptionally thin LMAs (10 μm) with NCM cathodes with acceptable mass loadings of 7.2 or 12.6 mg_{NCM} cm^{-2}, respectively.

To elucidate the origin of the significant difference in the performance of NCM/Li full cells between the uncoated and In/Li_xIn-coated (5 min) LMAs, operando electrochemical pressiometry measurements were carried out (Fig. 5) [65,66,71]. Volume changes occurring at the electrode materials during charge and discharge result in pressure changes of all-solid-state cells [72,73]. Because the volume change for LMAs is significantly larger than that for NCM cathodes (approximately 4–6%), the total pressure change of NCM/Li full cells follows that of LMAs [65,66,74]. Schematic of the cell configuration for the pressiometry measurements with the interfacial evolution is shown in Fig. 5a. The charge–discharge voltage profiles of the NCM/Li full cells for the uncoated and In/Li_xIn-coated LMAs at 0.5 C and 60 °C and the corresponding pressure changes (ΔP) are shown in Fig. 5b and c, respectively. The pressure change data for the In/Li_xIn-coated LMAs at extended cycles are provided in Figure S16. For both the uncoated and In/Li_xIn-coated LMAs, a linear relationship between charge and pressure change was observed, reflecting the dominance of the LMA volume change over the NCM pressure changes.

The discharge capacity and corresponding pressure change difference Δ(ΔP) during each discharge for the uncoated and In/Li_xIn-coated LMAs are plotted in Fig. 5d and e, respectively. Furthermore, the

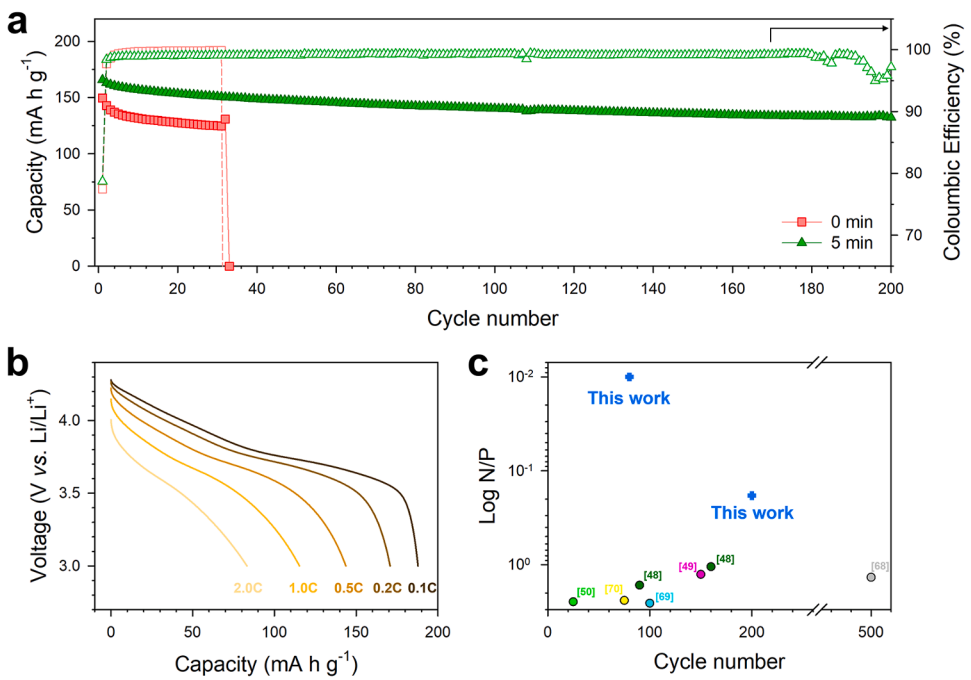

Fig. 4. Electrochemical performance results at 60 °C for NCM/Li all-solid-state full cells employing In/Li_xIn-coated thin LMAs. (a) Cycling performances of NCM/Li full cells at 1.0C for uncoated (0 min) and In/Li_xIn-coated (5 min) LMAs. (b) Discharge voltage profiles of NCM/Li full cells at varied discharge C-rates for In/Li_xIn-coated (5 min) LMAs. C-rate for charge was constant to be 0.1C. (c) Comparison of cycling performances for all-solid-state Li[*Ni*, *Co*,M*n*(*or Al*)]O_2/Li full cells with previous results in terms of N/P ratio.

pressure change differences were normalized with respect to the discharge capacity at each cycle (denoted as $\Delta(\Delta P)_Q$), and they are shown in Fig. 5f. Up to ~13 cycles, the $\Delta(\Delta P)_Q$ values for the uncoated and coated LMAs gradually decreased with almost identical values. While normal Li stripping/deposition for a bulk Li layer contributes to uniaxial pressure changes, Li filling defects, such as cracks and void spaces, cannot contribute to the uniaxial pressure increase (Figure S17). In this regard, the decreasing $\Delta(\Delta P)_Q$ indicates that the amount of Li stripped/deposited in the bulk layer was reduced, while the amount of Li filling defects was increased, that is, the penetrating growth of Li metal [37]. In addition, the effect of increasing the amount of Li/LPSCl side reactions forming Li_2S and Li_3P upon cycling cannot be excluded because the volume changes for these side reactions are lower than those for Li stripping/deposition ($Li_6PS_5Cl + 8Li \rightarrow 5Li_2S + Li_3P + LiCl$: $\Delta V = -18.4\%$, Supporting Information for further details). Therefore, by monitoring the changing $\Delta(\Delta P)_Q$ values, the growth mechanism of Li metal can be efficiently predicted. Interestingly, after 13 cycles, the uncoated LMAs showed a rapid decline in $\Delta(\Delta P)_Q$, in contrast to the coated LMAs, suggesting considerable Li penetration into the SE layers (Fig. 5f). This behavior is consistent with the abrupt cell failure by ISC at the 20th cycle for the uncoated LMAs, as shown in Fig. 5d. In particular, the uncoated LMAs showed stable capacity retention just before sudden failure, whereas $\Delta(\Delta P)_Q$ showed a distinct sign of significant Li penetration at several cycles prior to the failure. Therefore, the $\Delta(\Delta P)_Q$ value acts as an indicator of ISC. The $\Delta(\Delta P)_Q$ value for the coated LMAs gradually decreased up to ~30 cycles and was saturated to be 13.5 MPa g (A h)$^{-1}$; however, it increased in subsequent cycles (Fig. 5f). This result demonstrates the high tolerance of the In/Li_xIn-coated LMAs against penetrating Li growth, which is consistent with the electrochemical impedance spectroscopy (EIS) results of Li/LPSCl/c-Li symmetric cells.

The increasing pressure difference values after ~30th cycle for using the In/Li_xIn-coated LMAs (Fig. 5e, f) is also noteworthy. First, an inhomogeneous Li deposition/stripping could be the reason. An SEM image of LMA after 60 cycles of Li/LPSCl/c-Li symmetric cells and corresponding EDXS elemental maps of S, Fe, and O in Figure S18 represent an inhomogeneous chemical feature of the Li/LPSCl interfaces, implying highly inhomogeneous Li deposition/stripping. This interfacial reconfiguration upon cycling results in current constriction in decreased active surface area, which indicates increased uniaxial pressure changes (Figure S18e). Second, the dead Li formation could be another reason for the pressure difference increase. The penetrating Li fills the pores of the SE layer and may become inactive (or "dead") during the early cycles, which indicates that available pore spaces decrease. Then, the pressure changes could also increase.

Finally, the Li/LPSCl interfacial evolution was investigated by cross-sectional FESEM measurements of the NCM/Li all-solid-state cells (Fig. 6). In the pristine state, both the uncoated and coated (5 min) LMAs had an intimate interface with LPSCl (Fig. 6a and c). However, after 20 cycles, only the coated LMA maintained close interfacial contacts, whereas the uncoated LMA presented void spaces at the interface and a vertical crack that provided the path for the penetrating Li growth (Fig. 6b and d). This result is consistent with the electrochemical performance of the Li/LPSCl/c-Li symmetric cells and NCM/Li full cells. However, repeated charge–discharge cycling led to the migration of In throughout the LMAs (Figure S19), implying that LPSCl could be further decomposed by newly formed Li metal regions in every cycle. Indisputably, after the symmetric cell tests, it was observed that the In/Li_xIn layer partly vanished, and all the Li reservoirs were consumed by side reactions at the end of the cell life for both the uncoated and In/Li_xIn-coated LMAs (Figure S20). Specifically, the degraded surface coverage of the protective layer accelerates the side reaction and accordingly the Li plating/stripping reaction becomes more inhomogeneous, which leads to more vulnerability to internal short circuits [75–77]. The limited functionality of the In/Li_xIn coatings thus necessitates future research in the engineering of surface modifications. Furthermore, the pressiometry results over the entire range of cycles (Figure S16,) revealed an increase in the baseline pressure from ~75 h (23rd cycle), which indicates the expansion caused by continuous side reactions between Li and LPSCl [78,79]. The fast capacity decay of the NCM/Li all-solid-state full cells cycled at 0.5 C (Figure S15), starting at ~90th cycle would be related to those increased side reactions which should lead to increased cell polarization.

3. Conclusions

In summary, LMAs with thin (~10 μm thick) Li metal protected by a conformal and even In/Li_xIn layer were fabricated by wet-(electro) chemical routes. It was shown that the optimized In/Li_xIn coating on

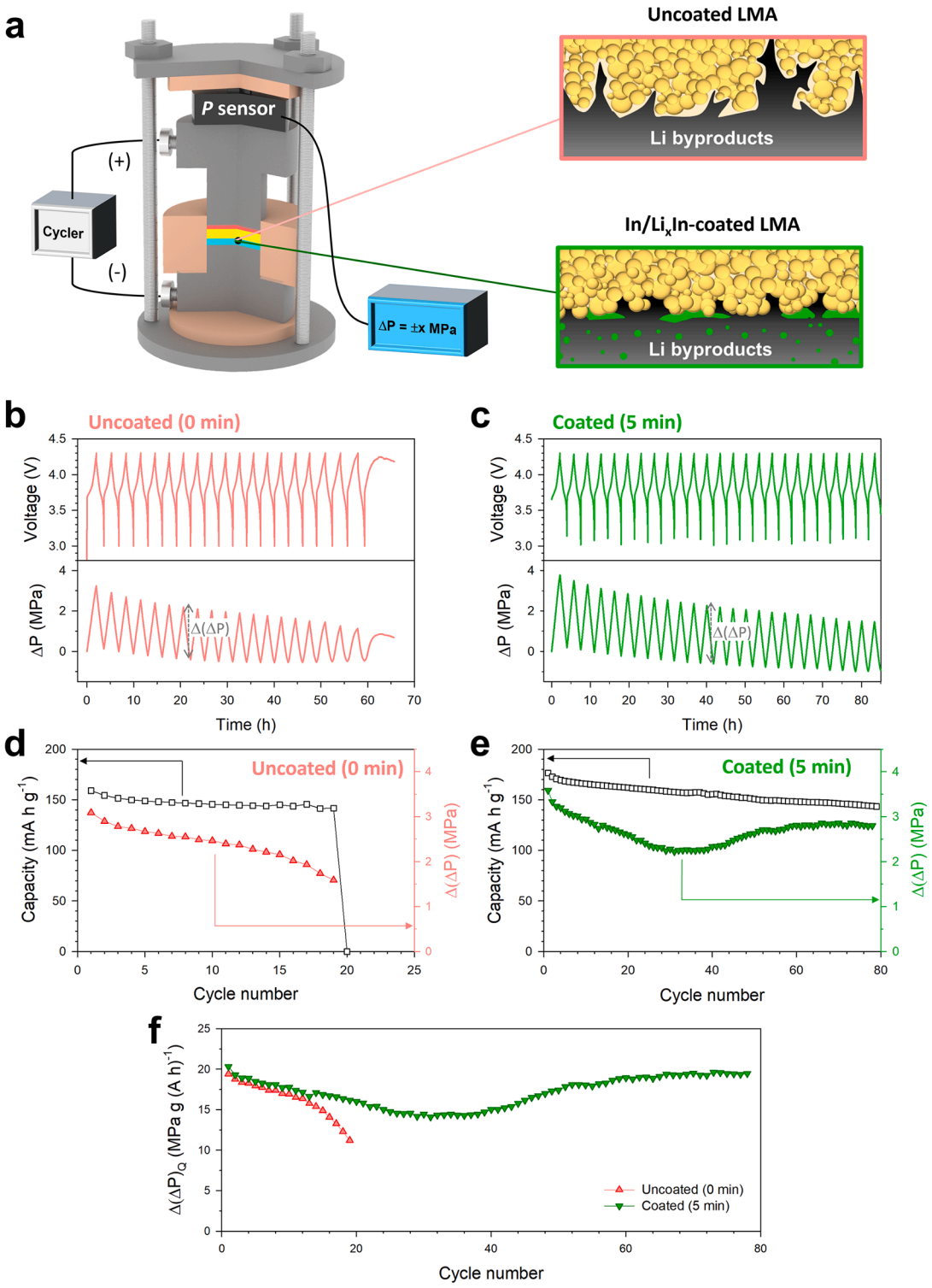

Fig. 5. Operando electrochemical pressiometry results of NCM/Li all-solid-state full cells at 0.5C and 60 °C for uncoated and In/Li$_x$In-coated thin LMAs. (a) Schematic of pressiometry measurements of NCM/Li all-solid-state full cells and interfacial evolution affected by the In/Li$_x$In protective coatings. Charge-discharge voltage profiles NCM/Li all-solid-state full cells and corresponding pressure changes for (b) uncoated (0 min) and (c) In/Li$_x$In-coated (5 min) thin LMAs. (d, e) Corresponding discharge capacities and pressure change difference (Δ(ΔP)) values as a function of cycle number. (f) Capacity-normalized pressure change difference (Δ(ΔP)$_Q$) as a function of cycle number.

LMAs, i.e., the plating reaction time of 5 min, was attributed to the minimal loss of Li during the electroless plating (13.0% and 9.8%, determined from the stripping tests and ICP-OES measurements) and the conformal coverage and homogeneity of the coatings. The significant improvements of thin LMAs by the In/Li$_x$In-coatings were successfully validated using both Li/LPSCl/c-Li symmetric cells and NCM/Li all-solid-state full cells with an N/P ratio of 1.53. The interfacial evolution varied with the In/Li$_x$In coating is illustrated in Fig. 7. Without the protective layer, repeated stripping/deposition of Li metal causes a severe side reaction with LPSCl. In addition, this results in void spaces at

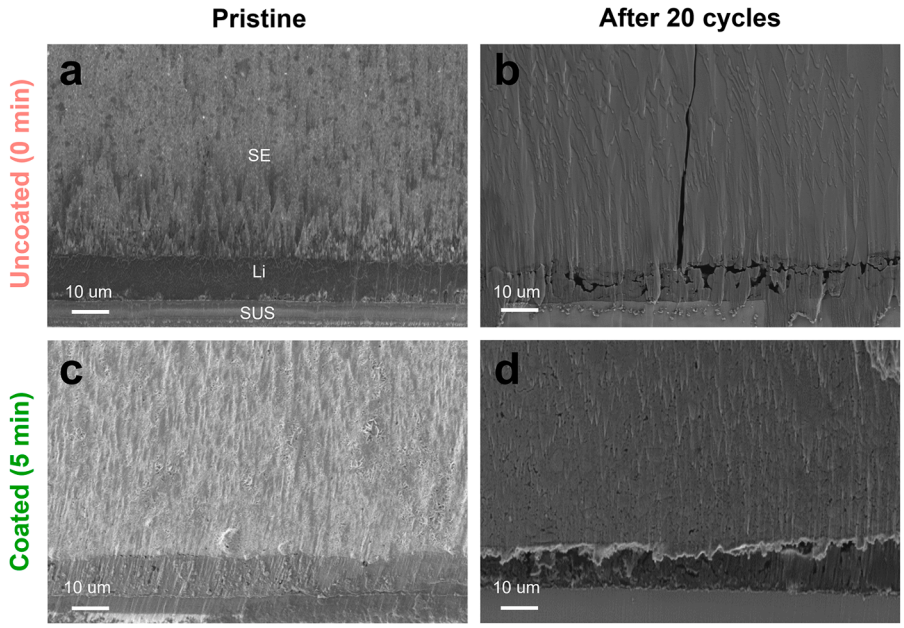

Fig. 6. Cross-sectional SEM images showing interfacial evolution at LPSCl/Li for NCM/Li all-solid-state full cells for (a, b) uncoated (0 min) and (c, d) In/Li_xIn-coated (5 min) LMAs before cycling (a, c) and after 20 cycles (b, d).

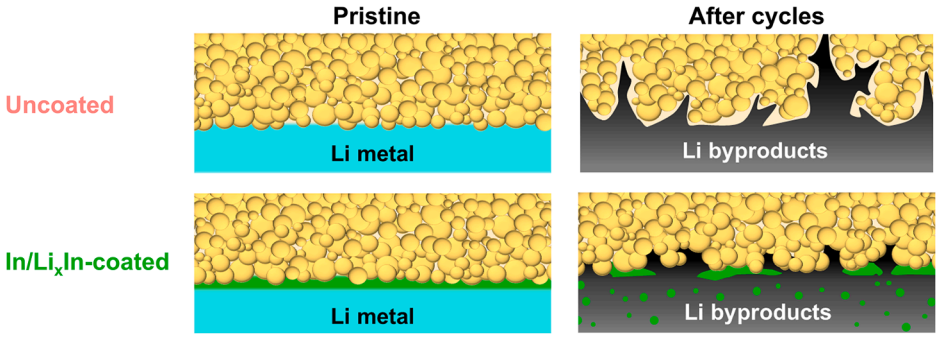

Fig. 7. Schematic illustrating the Li/LPSCl interfacial evolution for using uncoated and In/Li_xIn-coated LMAs.

the interfaces and cracks, which could accelerate or initiate the penetrating Li growth [80]. By avoiding direct contact between Li and LPSCl, there was a significant reduction in the amounts of side-reaction-derived byproducts and in the formation of cracks and interfacial void spaces. In particular, these features were demonstrated nondestructively by analyzing the capacity-normalized pressure change difference $\Delta(\Delta P_Q)$ in operando electrochemical pressiometry, which is the first identified indicator for Li metal plating mechanism. By monitoring $\Delta(\Delta P_Q)$ throughout cycles, the Li/(In/Li_xIn)/LPSCl interfacial evolution was successfully probed, and ISC was predicted several cycles prior to the apparent sign of cell failure. Furthermore, we illustrated the difference between the symmetric cell and full cell conditions, emphasizing the importance of the amount of the Li reservoir. Despite the promising features of In/Li_xIn protective layer in our results, the In/Li_xIn protective coating layers could not remain immobile upon repeated charge-discharge cycles, and the Li reservoir was eventually depleted. Therefore, further efforts to upgrade the strategy for protective layers are necessary for future studies to improve ASLMB performance, such as thickening the layer [81], applying a biphasic layer [41], and polymer interlayer [82,83] or polymer coating on SEs [84].

4. Experimental

4.1. Preparation of materials

LiFSI (Sigma Aldrich), In(TFSI)$_3$ (Sigma Aldrich), EC/DMC (1:1 v/v, Guotai Huarong New Chemical Materials Co., Ltd. Korea), and DEC (Guotai Huarong New Chemical Materials Co. Ltd. Korea) and DME (Guotai Huarong New Chemical Materials Co., Ltd. Korea) were used as received. LiFSI (3 M) dissolved in DME was used as the Li-plating solution. The Li metal counter electrode and SUS foil were immersed in the plating solution and electrically connected to the wire. By controlling the current density to 2 mA cm^{-2} and plating time to 3710 s, 10 μm thick Li metal was deposited on a SUS foil with an area of 100 × 100 mm^2. The as-electrodeposited LMA surface was rinsed with DME. For the electroless plating of In on electrodeposited LMAs, a solution of 12 mM In(TFSI)$_3$ in EC/DMC was prepared. Then, electrodeposited Li foils with a diameter of 12 mm were immersed in 2 mL of the In(TFSI)$_3$ solution for the targeted time. After the plating reaction, the LMA samples were rinsed with DEC and dried in an Ar-filled dry box prior to further use. NCM powders coated with $LiNbO_3$ (1.4 wt.%) via wet-chemical method using lithium ethoxide (99.95%, Sigma Aldrich) and niobium ethoxide (99.95%, Sigma Aldrich) were used [85]. L_6PS_5Cl powder (CIS Co., Ltd. Korea) with a Li^+ conductivity of 2.8 mS cm^{-1} at 30 °C, determined by the AC method using Ti/SE/Ti symmetric cells, was used as received.

4.2. Materials characterization

For XRD measurements, the samples were hermetically sealed using a Be window. They were mounted on a Rigaku MiniFlex 600 diffractometer and subjected to measurements using Cu K_α radiation (1.5406 Å) in the 2θ scanning range of 10°–80° with a step size of 0.02° at 40 kV and 15 mA. Cross-sectional FESEM images were obtained by cold polishing the samples at 4.5 kV for 10 h followed by 1.5 kV milling for 2 h with an Ar ion beam at −30 °C (JEOL, IB19510CP). FESEM images and corresponding EDX elemental maps were obtained using AURIGA (Carl Zeiss). The sample specimens were stored and transported using an air-isolation system holder to avoid exposure to ambient air. The amount of Li loss during the electroless In plating reaction, obtained by ICP-OES measurements (OPTIMA 8300) was determined for the plating solution collected after the reaction. Ex situ XPS measurements were performed with a monochromatic Al K_α source (1486.6 eV) at 12 kV and 6 mA using K-Alpha+ (Thermo Fisher Scientific). The samples were mounted on a sample holder in an Ar-filled glove box and transferred to XPS equipment without exposure to ambient air. The surface of sulfide SE pellets collected from the Li/L_6PS_5Cl/c-Li symmetric cells after 110 cycles was used for the XPS measurements.

4.3. Electrochemical characterization

All-solid-state cells with a diameter of 13 mm, comprising Ti rods as the current collectors and a polyaryletheretherketone mold were used. To fabricate all-solid-state Li/L_6PS_5Cl/c-Li symmetric cells, an LPSCl layer was formed by pelletizing 150 mg of LPSCl by pressing at 520 MPa for 3 min. Then, a working electrode (uncoated or coated LMA) with a diameter of 12 mm was attached to one side of the SE (LPSCl) layer, and $Li_{100}In$ (8:2 wt ratio, 500 μm corresponding to 100 mA h cm^{-2}, Honjo Metal. Co., Ltd.) counter electrode was placed on the other side of the SE layer. $Li_{100}In$ counter electrodes were utilized instead of pure Li metal to mitigate the ISC by the counter electrode. The entire assembly was pressed at a pressure of 30 MPa. After pre-cycling at 0.2 mA cm^{-2} for 1 h for each charge and discharge cycle during the first 10 cycles, galvanostatic cycling tests were carried out at 1.0 mA cm^{-2} for 1 h at each charge and discharge cycle. The EIS data were collected by using an amplitude of 7 mV and a frequency range from 7 MHz to 100 mHz on a VSP300 (Bio-Logic). The frequency range was set to minimize the alteration of the cells during the measurements while providing enough data for the impedance analysis. EIS measurements of the symmetric cells were performed before the galvanostatic cycling test and after 60, 110, and 210 cycles. Despite incomplete shape of the semi-circles, the fitting of the Nyquist plots was performed following the reported equivalent circuit and resistance components of Li symmetric cell [30, 59]. The NCM cathodes were prepared using a wet-slurry method. A mixture of NCM, LPSCl, NBR biner and conducting carbon additives (Super C65) in a weight ratio of 70: 27.5: 1.5: 1 was added to a slurry-processing solvent of benzyl acetate (99%, Sigma Aldrich) and coated on an carbon-Al current collector using the doctor-blade method. The cast slurry was dried under vacuum at 150 °C. After the SE layers were formed by pelletizing 150 mg of LPSCl powder under 70 MPa, cathodes were placed on one side of the SE layer and the entire assembly was pressed at 370 MPa. Finally, either uncoated or coated LMA was attached to the other side of the SE layer under a pressure of 70 MPa. All-solid-state full cells were cycled at 0.5 C or 1.0 C at 60 °C between 3.0–4.3 V. For operando pressiometry measurements, pressure sensors with a resolution of 0.1 kg (load cell, BONGSHIN) were placed in the ASLMB setup (Fig. 6a). The pressure changes during charging and discharging were monitored using in-house software. The capacity-normalized pressure change difference $\Delta(\Delta P_Q)$ was calculated by the following equation: $\Delta(\Delta P_Q) = \Delta(\Delta P)/Q_{discharge}$ where $Q_{discharge}$ is a discharge capacity at a corresponding cycle. All processes for fabricating the electrodes were conducted in an Ar-filled dry glove box. The mass loadings of NCM were 7.2 mg cm^{-2} for the cycling test and 12.6 mg cm^{-2} for the rate and pressiometry measurements.

Author statement

Haechannara Lim: Conceptualization, methodology, investigation, writing - original draft

Seunggo Jun: Conceptualization, methodology, investigation

Yong Bae Song: Investigation

Dr. Hongyeul Bae: Conceptualization, supervision

Dr. Jin Hong Kim: Conceptualization, supervision

Prof. Yoon Seok Jung: Conceptualization, supervision, writing – review & editing

Declaration of Competing Interest

The authors declare that they have no known competing financial interests or personal relationships that could have appeared to influence the work reported in this paper.

Acknowledgements

Haechannara Lim and Seunggoo Jun contributed equally to this work. This work was supported by the technology innovation program (20012216 and 20007045) funded by the Ministry of Trade, Industry & Energy (MOTIE, Korea) and by the Technology Development Program to Solve Climate Changes through the National Research Foundation of Korea (NRF) funded by the Ministry of Science, ICT & Future Planning (2017M1A2A2044501 and 2022M3J1A1085397).

Supplementary materials

Supplementary material associated with this article can be found, in the online version, at doi:10.1016/j.ensm.2022.05.050.

References

[1] V. Etacheri, R. Marom, R. Elazari, G. Salitra, D. Aurbach, Challenges in the development of advanced Li-ion batteries: a review, Energy Environ. Sci. 4 (2011) 3243, https://doi.org/10.1039/C1EE01598B.
[2] G. Jeong, Y.-.U. Kim, H. Kim, Y.-.J. Kim, H.-.J. Sohn, Prospective materials and applications for Li secondary batteries, Energy Environ. Sci. 4 (2011) 1986–2002, https://doi.org/10.1039/C0EE00831A.
[3] H. Li, Practical evaluation of Li-ion batteries, Joule 3 (2019) 911–914, https://doi.org/10.1016/j.joule.2019.03.028.
[4] X.B. Cheng, R. Zhang, C.Z. Zhao, Q. Zhang, Toward safe lithium metal anode in rechargeable batteries: a review, Chem. Rev. 117 (2017) 10403–10473, https://doi.org/10.1021/acs.chemrev.7b00115.
[5] D. Lin, Y. Liu, Y. Cui, Reviving the lithium metal anode for high-energy batteries, Nat. Nanotechnol. 12 (2017) 194–206, https://doi.org/10.1038/nnano.2017.16.
[6] S. Chen, F. Dai, M. Cai, Opportunities and challenges of high-energy lithium metal batteries for electric vehicle applications, ACS Energy Lett. 5 (2020) 3140–3151, https://doi.org/10.1021/acsenergylett.0c01545.
[7] Y. Shen, Y. Zhang, S. Han, J. Wang, Z. Peng, L. Chen, Unlocking the energy capabilities of lithium metal electrode with solid-state electrolytes, Joule 2 (2018) 1674–1689, https://doi.org/10.1016/j.joule.2018.06.021.
[8] J.W. Choi, D. Aurbach, Promise and reality of post-lithium-ion batteries with high energy densities, Nat. Rev. Mater. 1 (2016) 16013, https://doi.org/10.1038/natrevmats.2016.13.
[9] J. Kalhoff, G.G. Eshetu, D. Bresser, S. Passerini, Safer electrolytes for lithium-ion batteries: state of the art and perspectives, ChemSusChem 8 (2015) 2154–2175, https://doi.org/10.1002/cssc.201500284.
[10] K. Liu, Y.Y. Liu, D.C. Lin, A. Pei, Y. Cui, Materials for lithium-ion battery safety, Sci. Adv. 4 (2018) eaas9820, https://doi.org/10.1126/sciadv.aas9820.
[11] Y. Kato, S. Hori, T. Saito, K. Suzuki, M. Hirayama, A. Mitsui, M. Yonemura, H. Iba, R. Kanno, High-power all-solid-state batteries using sulfide superionic conductors, Nat. Energy 1 (2016) 16030, https://doi.org/10.1038/nenergy.2016.30.
[12] J. Janek, W.G. Zeier, A solid future for battery development, Nat. Energy 1 (2016) 16141, https://doi.org/10.1038/nenergy.2016.141.
[13] K.H. Park, Q. Bai, D.H. Kim, D.Y. Oh, Y. Zhu, Y. Mo, Y.S. Jung, Design strategies, practical considerations, and new solution processes of sulfide solid electrolytes for all-solid-state batteries, Adv. Energy Mater. 8 (2018), 1800035, https://doi.org/10.1002/aenm.201800035.
[14] A. Manthiram, X. Yu, S. Wang, Lithium battery chemistries enabled by solid-state electrolytes, Nat. Rev. Mater. 2 (2017) 16103, https://doi.org/10.1038/natrevmats.2016.103.

[15] Z. Zhang, Y. Shao, B. Lotsch, Y.-.S. Hu, H. Li, J. Janek, L.F. Nazar, C.-.W. Nan, J. Maier, M. Armand, L. Chen, New horizons for inorganic solid state ion conductors, Energy Environ. Sci. 11 (2018) 1945–1976, https://doi.org/10.1039/C8EE01053F.

[16] F. Han, A.S. Westover, J. Yue, X. Fan, F. Wang, M. Chi, D.N. Leonard, N.J. Dudney, H. Wang, C. Wang, High electronic conductivity as the origin of lithium dendrite formation within solid electrolytes, Nat. Energy 4 (2019) 187–196, https://doi.org/10.1038/s41560-018-0312-z.

[17] Y.S. Jung, D.Y. Oh, Y.J. Nam, K.H. Park, Issues and challenges for bulk-type all-solid-state rechargeable lithium batteries using sulfide solid electrolytes, Isr. J. Chem. 55 (2015) 472–485, https://doi.org/10.1002/ijch.201400112.

[18] K. Kerman, A. Luntz, V. Viswanathan, Y.-.M. Chiang, Z. Chen, Review—practical challenges hindering the development of solid state li ion batteries, J. Electrochem. Soc. 164 (2017) A1731–A1744, https://doi.org/10.1149/2.1571707jes.

[19] H.J. Deiseroth, S.T. Kong, H. Eckert, J. Vannahme, C. Reiner, T. Zaiss, M. Schlosser, Li6PS5X: a class of crystalline Li-rich solids with an unusually high Li+ mobility, Angew. Chem. Int. Ed. 47 (2008) 755–758, https://doi.org/10.1002/anie.200703900.

[20] P. Adeli, J.D. Bazak, K.H. Park, I. Kochetkov, A. Huq, G.R. Goward, L.F. Nazar, Boosting solid-state diffusivity and conductivity in lithium superionic argyrodites by halide substitution, Angew. Chem. Int. Ed. 58 (2019) 8681–8686, https://doi.org/10.1002/anie.201814222.

[21] S. Stramare, V. Thangadurai, W. Weppner, Lithium lanthanum titanates: a review, Chem. Mater. 15 (2003) 3974–3990, https://doi.org/10.1021/cm0300516.

[22] T. Asano, A. Sakai, S. Ouchi, M. Sakaida, A. Miyazaki, S. Hasegawa, Solid halide electrolytes with high lithium-ion conductivity for application in 4 V class bulk-type all-solid-state batteries, Adv. Mater. 30 (2018), 1803075, https://doi.org/10.1002/adma.201803075.

[23] H. Kwak, D. Han, J. Lyoo, J. Park, S.H. Jung, Y. Han, G. Kwon, H. Kim, S.T. Hong, K.W. Nam, Y.S. Jung, New cost-effective halide solid electrolytes for all-solid-state batteries: mechanochemically prepared Fe^{3+}-substituted Li_2ZrCl_6, Adv. Energy Mater. 11 (2021), 2003190, https://doi.org/10.1002/aenm.202003190.

[24] H. Kwak, S. Wang, J. Park, Y. Liu, K.T. Kim, Y. Choi, Y. Mo, Y.S. Jung, Emerging halide superionic conductors for all-solid-state batteries: design, synthesis, and practical applications, ACS Energy Lett. 7 (2022) 1776, https://doi.org/10.1021/acsenergylett.2c00438.

[25] L. Duchêne, A. Remhof, H. Hagemann, C. Battaglia, Status and prospects of hydroborate electrolytes for all-solid-state batteries, Energy Storage Mater. 25 (2020) 782–794, https://doi.org/10.1016/j.ensm.2019.08.032.

[26] S. Kim, H. Oguchi, N. Toyama, T. Sato, S. Takagi, T. Otomo, D. Arunkumar, N. Kuwata, J. Kawamura, S.-i. Orimo, A complex hydride lithium superionic conductor for high-energy-density all-solid-state lithium metal batteries, Nat. Commun. 10 (2019) 1081, https://doi.org/10.1038/s41467-019-09061-9.

[27] T. Krauskopf, F.H. Richter, W.G. Zeier, J. Janek, Physicochemical concepts of the lithium metal anode in solid-state batteries, Chem. Rev. 120 (2020) 7745–7794, https://doi.org/10.1021/acs.chemrev.0c00431.

[28] A. Banerjee, X. Wang, C. Fang, E.A. Wu, Y.S. Meng, Interfaces and Interphases in All-Solid-State Batteries with Inorganic Solid Electrolytes, Chem. Rev. 120 (2020) 6878–6933, https://doi.org/10.1021/acs.chemrev.0c00101.

[29] J. Kasemchainan, S. Zekoll, D. Spencer Jolly, Z. Ning, G.O. Hartley, J. Marrow, P. G. Bruce, Critical stripping current leads to dendrite formation on plating in lithium anode solid electrolyte cells, Nat. Mater. 18 (2019) 1105–1111, https://doi.org/10.1038/s41563-019-0438-9.

[30] S. Wenzel, S.J. Sedlmaier, C. Dietrich, W.G. Zeier, J. Janek, Interfacial reactivity and interphase growth of argyrodite solid electrolytes at lithium metal electrodes, Solid State Ion 318 (2018) 102–112, https://doi.org/10.1016/j.ssi.2017.07.005.

[31] J. Lau, R.H. DeBlock, D.M. Butts, D.S. Ashby, C.S. Choi, B.S. Dunn, Sulfide solid electrolytes for lithium battery applications, Adv. Energy Mater. 8 (2018), 1800933, https://doi.org/10.1002/aenm.201800933.

[32] Y. Zhu, X. He, Y. Mo, First principles study on electrochemical and chemical stability of solid electrolyte–electrode interfaces in all-solid-state Li-ion batteries, J. Mater. Chem. A 4 (2016) 3253–3266, https://doi.org/10.1039/C5TA08574H.

[33] J. Wu, S. Liu, F. Han, X. Yao, C. Wang, Lithium/sulfide all-solid-state batteries using sulfide electrolytes, Adv. Mater. 6 (2021), 2000751, https://doi.org/10.1002/adma.202000751.

[34] A. Kato, H. Kowada, M. Deguchi, C. Hotehama, A. Hayashi, M. Tatsumisago, XPS and SEM analysis between Li/Li_3PS_4 interface with Au thin film for all-solid-state lithium batteries, Solid State Ion 322 (2018) 1–4, https://doi.org/10.1016/j.ssi.2018.04.011.

[35] F. Zhao, Q. Sun, C. Yu, S. Zhang, K. Adair, S. Wang, Y. Liu, Y. Zhao, J. Liang, C. Wang, X. Li, X. Li, W. Xia, R. Li, H. Huang, L. Zhang, S. Zhao, S. Lu, X. Sun, Ultrastable anode interface achieved by fluorinating electrolytes for all-solid-state Li metal batteries, ACS Energy Lett. 5 (2020) 1035–1043, https://doi.org/10.1021/acsenergylett.0c00207.

[36] N. von Aspern, G.V. Roschenthaler, M. Winter, I. Cekic-Laskovic, Fluorine and lithium: ideal partners for high-performance rechargeable battery electrolytes, Angew. Chem. Int. Ed. 58 (2019) 15978–16000, https://doi.org/10.1002/anie.201901381.

[37] X. Ji, S. Hou, P. Wang, X. He, N. Piao, J. Chen, X. Fan, C. Wang, Solid-state electrolyte design for lithium dendrite suppression, Adv. Mater. 32 (2020), e2002741, https://doi.org/10.1002/adma.202002741.

[38] X.L. Fan, X. Ji, F.D. Han, J. Yue, J. Chen, L. Chen, T. Deng, J.J. Jiang, C.S. Wang, Fluorinated solid electrolyte interphase enables highly reversible solid-state Li metal battery, Sci. Adv. 4 (2018) 9245, https://doi.org/10.1126/sciadv.aau9245.

[39] K. Fu, Y. Gong, B. Liu, Y. Zhu, S. Xu, Y. Yao, W. Luo, C. Wang, D. Lacey Steven, J. Dai, Y. Chen, Y. Mo, E. Wachsman, L. Hu, Toward garnet electrolyte–based Li metal batteries: an ultrathin, highly effective, artificial solid-state electrolyte/metallic Li interface, Sci. Adv. 3 (2017), e1601659, https://doi.org/10.1126/sciadv.1601659.

[40] Y. Liu, C. Li, B. Li, H. Song, Z. Cheng, M. Chen, P. He, H. Zhou, Germanium thin film protected lithium aluminum germanium phosphate for solid-state Li batteries, Adv. Energy Mater. 8 (2018), 1702374, https://doi.org/10.1002/aenm.201702374.

[41] H. Wan, S. Liu, T. Deng, J. Xu, J. Zhang, X. He, X. Ji, X. Yao, C. Wang, Bifunctional interphase-enabled $Li_{10}GeP_2S_{12}$ electrolytes for lithium–sulfur battery, ACS Energy Lett. 6 (2021) 862–868, https://doi.org/10.1021/acsenergylett.0c02617.

[42] Y.-.G. Lee, S. Fujiki, C. Jung, N. Suzuki, N. Yashiro, R. Omoda, D.-.S. Ko, T. Shiratsuchi, T. Sugimoto, S. Ryu, J.H. Ku, T. Watanabe, Y. Park, Y. Aihara, D. Im, I.T. Han, High-energy long-cycling all-solid-state lithium metal batteries enabled by silver–carbon composite anodes, Nat. Energy 5 (2020) 299–308, https://doi.org/10.1038/s41560-020-0575-z.

[43] K.B. Hatzell, X.C. Chen, C.L. Cobb, N.P. Dasgupta, M.B. Dixit, L.E. Marbella, M. T. McDowell, P.P. Mukherjee, A. Verma, V. Viswanathan, A.S. Westover, W. G. Zeier, Challenges in lithium metal anodes for solid-state batteries, ACS Energy Lett. 5 (2020) 922–934, https://doi.org/10.1021/acsenergylett.9b02668.

[44] S. Randau, D.A. Weber, O. Kötz, R. Koerver, P. Braun, A. Weber, E. Ivers-Tiffée, T. Adermann, J. Kulisch, W.G. Zeier, F.H. Richter, J. Janek, Benchmarking the performance of all-solid-state lithium batteries, Nat. Energy 5 (2020) 259–270, https://doi.org/10.1038/s41560-020-0565-1.

[45] H. Chen, Y. Yang, D.T. Boyle, Y.K. Jeong, R. Xu, L.S. de Vasconcelos, Z. Huang, H. Wang, H. Wang, W. Huang, H. Li, J. Wang, H. Gu, R. Matsumoto, K. Motohashi, Y. Nakayama, K. Zhao, Y. Cui, Free-standing ultrathin lithium metal–graphene oxide host foils with controllable thickness for lithium batteries, Nat. Energy 6 (2021) 790–798, https://doi.org/10.1038/s41560-021-00833-6.

[46] M.J. Wang, E. Carmona, A. Gupta, P. Albertus, J. Sakamoto, Enabling "lithium-free" manufacturing of pure lithium metal solid-state batteries through in situ plating, Nat. Commun. 11 (2020) 5201, https://doi.org/10.1038/s41467-020-19004-4.

[47] R. Sahore, Z. Du, X.C. Chen, W.B. Hawley, A.S. Westover, N.J. Dudney, Practical considerations for testing polymer electrolytes for high-energy solid-state batteries, ACS Energy Lett. 6 (2021) 2240–2247, https://doi.org/10.1021/acsenergylett.1c00810.

[48] Y. Wang, J. Ju, S. Dong, Y. Yan, F. Jiang, L. Cui, Q. Wang, X. Han, G. Cui, Facile design of sulfide-based all solid-state lithium metal battery: in situ polymerization within self-supported porous argyrodite skeleton, Adv. Funct. Mater. 31 (2021), 2101523, https://doi.org/10.1002/adfm.202101523.

[49] Z. Zhang, L. Wu, D. Zhou, W. Weng, X. Yao, Flexible sulfide electrolyte thin membrane with ultrahigh ionic conductivity for all-solid-state lithium batteries, Nano Lett. 21 (2021) 5233–5239, https://doi.org/10.1021/acs.nanolett.1c01344.

[50] J.H. Woo, J.E. Trevey, A.S. Cavanagh, Y.S. Choi, S.C. Kim, S.M. George, K.H. Oh, S.-.H. Lee, Nanoscale interface modification of $LiCoO_2$ by Al_2O_3 atomic layer deposition for solid-state Li batteries, J. Electrochem. Soc. 159 (2012) A1120–A1124, https://doi.org/10.1149/2.085207jes.

[51] R. Chen, Q. Li, X. Yu, L. Chen, H. Li, Approaching practically accessible solid-state batteries: stability issues related to solid electrolytes and interfaces, Chem. Rev. 120 (2020) 6820–6877, https://doi.org/10.1021/acs.chemrev.9b00268.

[52] S. Wang, H. Xu, W. Li, A. Dolocan, A. Manthiram, Interfacial chemistry in solid-state batteries: formation of interphase and its consequences, J. Am. Chem. Soc. 140 (2018) 250–257, https://doi.org/10.1021/jacs.7b09531.

[53] S. Choudhury, Z. Tu, S. Stalin, D. Vu, K. Fawole, D. Gunceler, R. Sundararaman, L. A. Archer, Electroless formation of hybrid lithium anodes for fast interfacial ion transport, Angew. Chem. Int. Ed. 56 (2017) 13070–13077, https://doi.org/10.1002/anie.201707754.

[54] A.J. Bard, L.R. Faulkner, Electrochemical Methods: Fundamentals and Applications, John Wiley & Sons, Inc., New York, 2001.

[55] Y.-.H. Chung, C.-.W. Lee, Electrochemical behaviors of Indium, J. Electrochem. Sci. Technol. 3 (2012) 1–13, https://doi.org/10.5229/JECST.2012.3.1.1.

[56] X. Liang, Q. Pang, I.R. Kochetkov, M.S. Sempere, H. Huang, X. Sun, L.F. Nazar, A facile surface chemistry route to a stabilized lithium metal anode, Nat. Energy 2 (2017), https://doi.org/10.1038/nenergy.2017.119.

[57] K. Kanamura, H. Tomura, S. Shiraishi, Z.I. Takehara, XPS analysis of lithium surfaces following immersion in various solvents containing $LiBF_4$, J. Electrochem. Soc. 142 (1995) 340–347, https://doi.org/10.1149/1.2044000.

[58] R.W. Hewitt, N. Winograd, Oxidation of polycrystalline indium studied by x-ray photoelectron spectroscopy and static secondary ion mass spectroscopy, Int. J. Appl. Phys. 51 (1980) 2620, https://doi.org/10.1063/1.327991.

[59] L.M. Riegger, R. Schlem, J. Sann, W.G. Zeier, J. Janek, Lithium-metal anode instability of the superionic halide solid electrolytes and the implications for solid-state batteries, Angew. Chem. Int. Ed. 60 (2021) 6718–6723, https://doi.org/10.1002/anie.202015238.

[60] C.-Z.Zhao Y.Lu, H. Yuan, X.-B. Cheng, J.-Q. Huang, Q. Zhang, Critical current density in solid-state lithium metal batteries: mechanism, influences, and strategies, Adv. Funct. Mater. 31 (2021), 2009925, https://doi.org/10.1002/adfm.202009925.

[61] S. Luo, Z. Wang, X. Li, X. Liu, H. Wang, W. Ma, L. Zhang, L. Zhang, L. Zhu, X. Zhang, Growth of lithium-indium dendrites in all-solid-state lithium-based batteries with sulfide electrolyte, Nat. Commun. 12 (2021) 6968, https://doi.org/10.1038/s41467-021-27311-7.

[62] Y. Lu, C.-.Z. Zhao, R. Zhang, H. Yuan, L.-.P. Hou, Z.-.H. Fu, X. Chen, J.-.Q. Huang, Q. Zhang, The carrier transition from Li atoms to Li vacancies in solid-state lithium alloy anodes, Sci. Adv. 7 (2021) eabi5520, 10.1126/sciadv.abi5520.

[63] K.N. Wood, K.X. Steirer, S.E. Hafner, C. Ban, S. Santhanagopalan, S.-.H. Lee, G. Teeter, Operando X-ray photoelectron spectroscopy of solid electrolyte interphase formation and evolution in Li_2S-P_2S_5 solid-state electrolytes, Nat. Commun. 9 (2018) 2490, https://doi.org/10.1038/s41467-018-04762-z.

[64] J. Auvergniot, A. Cassel, D. Foix, V. Viallet, V. Seznec, R. Dedryvère, Redox activity of argyrodite Li_6PS_5Cl electrolyte in all-solid-state Li-ion battery: an XPS study, Solid State Ion 300 (2017) 78–85, https://doi.org/10.1016/j.ssi.2016.11.029.

[65] S.H. Jung, U.H. Kim, J.H. Kim, S. Jun, C.S. Yoon, Y.S. Jung, Y.K. Sun, Ni-rich layered cathode materials with electrochemo-mechanically compliant microstructures for all-solid-state Li batteries, Adv. Energy Mater. 10 (2020), 1903360, https://doi.org/10.1002/aenm.201903360.

[66] Y. Han, S.H. Jung, H. Kwak, S. Jun, H.H. Kwak, J.H. Lee, S.T. Hong, Y.S. Jung, Single- or poly-crystalline Ni-rich layered cathode, sulfide or halide solid electrolyte: which will be the winners for all-solid-state batteries? Adv. Energy Mater. 11 (2021), 2100126 https://doi.org/10.1002/aenm.202100126.

[67] P. Albertus, S. Babinec, S. Litzelman, A. Newman, Status and challenges in enabling the lithium metal electrode for high-energy and low-cost rechargeable batteries, Nat. Energy 3 (2018) 16–21, https://doi.org/10.1038/s41560-017-0047-2.

[68] Z. Zhang, S. Chen, J. Yang, J. Wang, L. Yao, X. Yao, P. Cui, X. Xu, Interface *re*-engineering of $Li_{10}GeP_2S_{12}$ electrolyte and lithium anode for all-solid-state lithium batteries with ultralong cycle life, ACS Appl. Mater. Interfaces 10 (2018) 2556–2565, https://doi.org/10.1021/acsami.7b16176.

[69] J. Zhang, H. Zhong, C. Zheng, Y. Xia, C. Liang, H. Huang, Y. Gan, X. Tao, W. Zhang, All-solid-state batteries with slurry coated $LiNi_{0.8}Co_{0.1}Mn_{0.1}O_2$ composite cathode and Li_6PS_5Cl electrolyte: effect of binder content, J. Power Sources 391 (2018) 73–79, https://doi.org/10.1016/j.jpowsour.2018.04.069.

[70] J.M. Whiteley, J.H. Woo, E. Hu, K.-.W. Nam, S.-.H. Lee, Empowering the lithium metal battery through a silicon-based superionic conductor, J. Electrochem. Soc. 161 (2014) A1812–A1817, https://doi.org/10.1149/2.0501412jes.

[71] S. Jun, Y.J. Nam, H. Kwak, K.T. Kim, D.Y. Oh, Y.S. Jung, Operando differential electrochemical pressiometry for probing electrochemo-mechanics in all-solid-state batteries, Adv. Funct. Mater. 30 (2020), 2002535, https://doi.org/10.1002/adfm.202002535.

[72] R. Koerver, W. Zhang, L. de Biasi, S. Schweidler, A.O. Kondrakov, S. Kolling, T. Brezesinski, P. Hartmann, W.G. Zeier, J. Janek, Chemo-mechanical expansion of lithium electrode materials – on the route to mechanically optimized all-solid-state batteries, Energy Environ. Sci. 11 (2018) 2142–2158, https://doi.org/10.1039/C8EE00907D.

[73] H. Michael, Jervis R, D.J.L. Brett, P.R. Shearing, Developments in dilatometry for characterisation of electrochemical devices, Batter. Supercaps. 4 (2021) 1378–1396, https://doi.org/10.1002/batt.202100027.

[74] A.O. Kondrakov, A. Schmidt, J. Xu, H. Geßwein, R. Mönig, P. Hartmann, H. Sommer, T. Brezesinski, J. Janek, Anisotropic lattice strain and mechanical degradation of high- and low-nickel NCM cathode materials for Li-ion batteries, J. Phys. Chem. 121 (2017) 3286–3294, https://doi.org/10.1021/acs.jpcc.6b12885.

[75] W. Feng, X. Dong, Z. Lai, X. Zhang, Y. Wang, C. Wang, J. Luo, Y. Xia, Building an interfacial framework: Li/garnet interface stabilization through a Cu_6Sn_5 layer, ACS Energy Lett. 4 (2019) 1725–1731, https://doi.org/10.1021/acsenergylett.9b01158.

[76] H. Zhou, S. Yu, H. Liu, P. Liu, Protective coatings for lithium metal anodes: recent progress and future perspectives, J. Power Sources 450 (2020), 227632, https://doi.org/10.1016/j.jpowsour.2019.227632.

[77] Y. Zhu, J. Xie, A. Pei, B. Liu, Y. Wu, D. Lin, J. Li, H. Wang, H. Chen, J. Xu, A. Yang, Wu C.-L, H. Wang, W. Chen, Y. Cui, Fast lithium growth and short circuit induced by localized-temperature hotspots in lithium batteries, Nat. Commun. 10 (2019) 2067, https://doi.org/10.1038/s41467-019-09924-1.

[78] C. Lee, S.Y. Han, J.A. Lewis, P.P. Shetty, D. Yeh, Y. Liu, E. Klein, H.-.W. Lee, M. T. McDowell, Stack pressure measurements to probe the evolution of the lithium–solid-state electrolyte interface, ACS Energy Lett. 6 (2021) 3261–3269, https://doi.org/10.1021/acsenergylett.1c01395.

[79] M. Suyama, A. Kato, A. Sakuda, A. Hayashi, M. Tatsumisago, Lithium dissolution/deposition behavior with Li_3PS_4-LiI electrolyte for all-solid-state batteries operating at high temperatures, Electrochim. Acta 286 (2018) 158–162, https://doi.org/10.1016/j.electacta.2018.07.227.

[80] M. Li, D. Zhou, C. Wang, W. Weng, M. Jiang, G. Liu, X. Yao, H. He, In situ formed Li-Ag alloy interface enables $Li_{10}GeP_2S_{12}$-based all-solid-state lithium batteries, ACS Appl. Mater. Interfaces 13 (2021) 50076–50082, https://doi.org/10.1021/acsami.1c16356.

[81] M. Otoyama, M. Suyama, C. Hotehama, H. Kowada, Y. Takeda, K. Ito, A. Sakuda, M. Tatsumisago, A. Hayashi, Visualization and control of chemically induced crack formation in all-solid-state lithium-metal batteries with sulfide electrolyte, ACS Appl. Mater. Interfaces 13 (2021) 5000–5007, https://doi.org/10.1021/acsami.0c18314.

[82] J.Y. Liang, X.X. Zeng, X.D. Zhang, T.T. Zuo, M. Yan, Y.X. Yin, J.L. Shi, X.W. Wu, Y. G. Guo, L.J. Wan, Engineering janus interfaces of ceramic electrolyte via distinct functional polymers for stable high-voltage Li-metal batteries, J. Am. Chem. Soc. 141 (2019) 9165–9169, https://doi.org/10.1021/jacs.9b03517.

[83] H. Duan, M. Fan, W.P. Chen, J.Y. Li, P.F. Wang, W.P. Wang, J.L. Shi, Y.X. Yin, L. J. Wan, Y.G. Guo, Extended electrochemical window of solid electrolytes via heterogeneous multilayered structure for high-voltage lithium metal batteries, Adv. Mater. 31 (2019), e1807789, https://doi.org/10.1002/adma.201807789.

[84] G. Liu, J. Shi, M. Zhu, W. Weng, L. Shen, J. Yang, X. Yao, Ultra-thin free-standing sulfide solid electrolyte film for cell-level high energy density all-solid-state lithium batteries, Energy Storage Mater. 38 (2021) 249–254, https://doi.org/10.1016/j.ensm.2021.03.017.

[85] D.Y. Oh, Y.J. Nam, K.H. Park, S.H. Jung, K.T. Kim, A.R. Ha, Y.S. Jung, Slurry-fabricable Li^+-conductive polymeric binders for practical all-solid-state lithium-ion batteries enabled by solvate ionic liquids, Adv. Energy. Mater. 9 (2019), 1802927, https://doi.org/10.1002/aenm.201802927.